Effect of Electron Beam Remelting Treatments on the Microstructure and Properties of Atmospheric Plasma Sprayed Tungsten Coatings

Wei-Bing Liao[1] · Zheng-Yang Liu[1] · Min-Jun He[1] · Chuangshi Feng[1] · Fan Wang[1] · Jianjun Huang[1]

Abstract Atmospheric plasma-sprayed tungsten coating is one of the most prospective plasma-facing materials used in the first wall of nuclear fusion devices since its low tritium inventory, good compatibility, and cost-effective. However, there are still some issues need to be addressed for the atmospheric plasma-sprayed tungsten coatings, such as high porosity and low thermal diffusivity. In this study, electron beam remelting treatments (EBRTs) have been used to modify the surface microstructure of atmospheric plasma-sprayed tungsten coatings, and the properties of the coatings such as porosity, oxygen content, microhardness, wear, and corrosion resistance are characterized and studied systematically. The experimental results revealed that a compact remelted layer with a columnar crystal structure is formed on the surface of the tungsten coating by EBRTs, and the porosity and oxygen content have been significantly reduced. The microhardness of the tungsten coating has nearly doubled after EBRTs. Comparing with the as-sprayed tungsten coating, the wear and corrosion resistance of the electron beam treated tungsten coatings have been considerably improved. Moreover, the thermal diffusivity has also been significantly enhanced.

Keywords electron beam remelting · hardness · microstructure · thermal diffusivity · tungsten coating

✉ Jianjun Huang
huangjj@szu.edu.cn

Wei-Bing Liao
liaowb@szu.edu.cn

1 College of Physics and Optoelectronic Engineering, Shenzhen University, Shenzhen 518060, China

Introduction

Owing to the advantages of high melting temperature, low tritium inventory, good compatibility with fusion plasma, and low erosion rate under plasma loading (Ref 1-3), tungsten (W) is one of the most prospective plasma-facing materials for use in the first wall of nuclear fusion devices, which imposes very demanding operation conditions such as comprising incident particles and heat flux from the plasma (Ref 4-8). It is hard to use W block directly for the first wall as it's a brittle feature. At present, the W-wall is covered by a thin W coating on graphite and carbon fiber composite tiles, and these W coatings are commonly fabricated by traditional deposition techniques (Ref 9-11), among which atmospheric plasma spraying (APS) technique has attracted much more attention since its high deposition efficiency, flexible deposition shapes, in-situ repair and cost-effective (Ref 12-14). However, with regard to the application of the atmospheric plasma-sprayed W coatings, there are still many problems to be solved, such as high porosity and oxide content, which can significantly reduce the mechanical erosion and corrosion resistance and influence the quality of the sprayed coatings (Ref 15, 16). Many efforts have been devoted to improve the W coatings' microstructures and properties by decreasing the powder size, annealing, introducing compliant layers, and laser remelting (Ref 17-20). These methods have enhanced the W coating performance to some extent, but the microstructures and physical properties are not controllable. Nowadays, electron beam remelting treatments (EBRTs) are being widely used in materials engineering due to their high energy density, good thermal isolation, and reduced oxidation (Ref 21, 22). It is an effective technique in melting high-temperature metallic powders to obtain specific parts in complex geometry, such as Ti-6Al-

4V blades, tungsten alloys, and thermal barrier coatings (Ref 23-28). However, the effects of EBRTs on the microstructure and properties of the as-sprayed W coatings have not been studied/investigated. In this study, we conducted EBRTs on the surface of the as-sprayed W coatings in two different ways for comparison to improve their physical properties: one treated in a momentary time and the other in a sustained time. Moreover, the W coatings' microstructure, oxygen content, porosity, microhardness, wear, and corrosion resistances, and thermal diffusivity before and after EBRTs were investigated in contrast. It adopts a new controllable and effective method of EBRTs to improve the surface performance of the first wall W coating and provides a novel way for the development and application of atmospheric plasma-sprayed W coating materials. In addition, it will also provide important theoretical and experimental guidance in the electron beam surface modification of other coating materials.

Experimental Methods

Experimental Procedures of EBRTs on W Coatings

The whole procedure of EBRTs on atmospheric plasma sprayed W coatings are schematically illustrated in Fig. 1. Pure W coatings with an average thickness of $\sim$ 500 μm were sprayed on 316L steel substrates via APS system (SG-100, PRAXAIR, USA) using commercial W powders (Anhui Kerun Nano Technology, China) with a particle size of $\sim$ 10 μm. In order to ensure the smooth deposition, the W powders were dried at 150 °C over 2 h before the deposition and kept heating during the powder feeding. The spraying power was set to be 22 kW (44 V and 500 A) with a scanning rate of 200 mm/s and a spraying distance of 80 mm from the substrates. To ensure the continuity and stability of the spraying process, argon was used as primary, and carrier gas with a flow rate of 56.5 L/min and 17.5 L/min, respectively, and hydrogen was used as the second gas with a flow rate of 3.6 L/min. The W powder feed rate was 20 g/min. The number of the passes was 80, and a whole thickness of 500 μm was obtained, with an average thickness of 6.25 μm per pass, and the spraying parameters are listed in Table 1. To improve the quality of the tungsten coatings, the as-sprayed W coatings (named S0) were then treated through a raster scanning electron beam system (SEB-100A, STRONG, China), which can be set in different treat patterns to meet experimental requirements. In this study, since the treating time and the heat flux were considered the critical influencing factors, the experimental treatment was divided into two groups of samples for the investigation of the influence of EBRTs on the W coatings systemically. One group of samples was
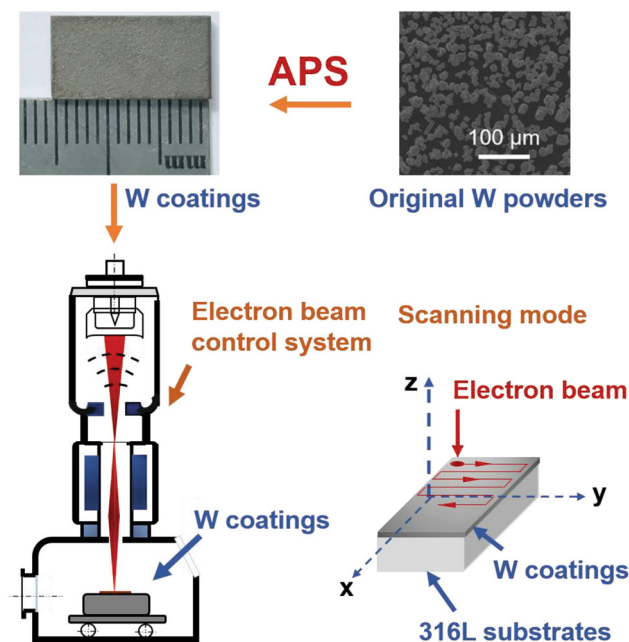

Fig. 1 Schematic illustrations of the whole procedures of EBRTs on the plasma sprayed W coatings

treated with a momentary time of 500 ms and a heat flux of 43.63 MW/m^2 (named S1), while the other group was treated with a sustained time of 6000 ms and a relatively low heat flux of 13.75 MW/m^2 (named S2), as listed in Table 2. During the whole procedure of EBRTs, the electron beam spot diameter was set to 1 mm, with a scanning line frequency of 5000 s^{-1}, and the selected area of the W coating was treated 78 times per second. The vacuum level for the EBRTs was less than 5×10^{-2} Pa.

Characterization of Microstructures and Phases

Microstructures of the original W powders and sprayed coatings were characterized by high-resolution scanning electron microscopy (SEM; FEI APREO S(A5-112), Hitachi, Japan), and oxygen contents of the sprayed coating surfaces were analyzed by the oxygen-nitrogen analyzer (ONH836, LECO, USA) under the test power of 5500 W. The final porosities of S0, S1, and S2 coatings were measured and calculated through ImageJ software (Ref 29), using the morphologies of the polished cross-sections. More than three morphologies for each sample were used to calculate the porosity of the coating. The surface roughness was measured by a profilometer (Bruker, Dektak XT, Germany) with a scan length of 2000 μm in 40 s. The phase information was identified by high-resolution X-ray diffraction (XRD; X′Pert-Pro, Philips, Netherlands) using Cu Kα radiation (λ = 0.154056 nm), with a scanning rate of 2.4°/min ranging from 20° to 90°.

Table 1 Deposition parameters for the pure W coatings prepared by APS technique

Voltage	Current	Primary gas (Ar)	Secondary gas (H$_2$)	Carrier gas (Ar)	Spraying distance	Powder feed rate	Gun scanning rate
44 V	500 A	56.5 L/min	3.6 L/min	17.5 L/min	80 mm	20 g/min	200 mm/s

Table 2 EBRTs parameters for the pure W coatings

Samples	Heat flux density, MW/m^2	Treating time, ms
S0	0	0
S1	43.63	500
S2	13.75	6000

S0: as-sprayed samples; S1: samples treated with a momentary time; S2: samples treated with a sustained time

Mechanical and physical properties

The Vickers microhardness of the coating was measured via microhardness tester (FT-ARS ver.1.19.0, Future-Tech Corp, Japan) with a load of 1 N for 10 s at ambient temperature. Before tests, sample cross-sections were ground and polished to ensure surface smoothness required for testing, and a W bulk sample was used for a control group. All the microhardness test points were conducted on the cross-sections of the samples near the coating surface. The surface wear resistance of the coatings was tested via a sandblasting machine (AMS7092C, AMS, China), using alumina particles with a size of 40-60 μm under 0.4 MPa pressure for 20 s. To ensure that the wear resistance could be reflected directly by the mass loss, the sandblasting area of each sample was controlled to be 15 mm × 1 mm. The angle of incidence of the blasting media on the coating surface was 30°. Electrochemical corrosion experiments of the coatings were conducted by electrode electrochemical workstation with three electrodes (CHI760E, CHI, China). The tests were processed in 3.5 wt.% NaCl solution at room temperature with a scanning rate of 1 mV/s from − 0.5 to 1.5 V. The open circuit potential was from − 0.1 to 0.1 V. Furthermore, the coatings were separated from the 316L steel substrate and made into specific flakes with a diameter of about 25 mm and thickness of 1 mm. Then the thermal diffusivity was measured by the flash method through the thermal conductivity instrument (LFA467, NETZSCH Gerätebau GmbH, Germany) at 100, 200, and 300 °C, respectively. During the test of the thermal diffusivity, a laser heat pulse was added to one side of the sample, and the relationship of time and temperature was measured on the other side. Each sample was tested three times, and the average value was calculated.

Results and Discussion

Microstructures of the W Coatings Before and After EBRTs

Figure 2 shows the detailed microstructures of the W coatings before and after EBRTs in comparison. For the as-sprayed W coating, S0 presents a rough surface (Fig. 2a). And from the cross-section shown in Fig. 2(b) and (c), it can be seen that a lot of pores and typical small lamellar structures with a thickness of about 3.2 μm exist in the as-sprayed W coating, which is the typical characteristic structure and has been found in previous studies (Ref 30). The formation of this feature microstructure is mainly because the melting W particles are periodically deposited on the substrate directly during the APS fabrication of the coating. After EBRTs in a momentary time, a thin remelted layer is formed on the surface of the W coating, and some clear grains with a size of about 50-100 μm can be observed in S1 (Fig. 2d). The number of pores is reduced, and some initial columnar structures with a thickness of ~ 10 μm start to grow on the surface, as shown in Fig. 2(e) and (f). Due to a momentary treated time, it is challenging to heat the whole sample uniformly. As a result, some lamellar structures and obvious pores remained in S1, and the remelted layer was on a relatively small scale. Furthermore, after EBRTs in a sustained time, a smooth surface of about 39 μm thick and prominent interface can be observed in S2, as shown in Fig. 2(h). The pores and lamellar structures start to disappear significantly in the remelted area (Fig. 2i), and the columnar crystalline grows perpendicular to the surface and finally reached a large grain size of ~ 200 μm (Fig. 2g and i). This is due to the stable and continuous electron beam processing environment, which provides a sustain condition for the grains to grow gradually. It was observed that the value of the surface roughness (R_a) of the W coating was reduced dramatically after EBRTs, as listed in Table 3. The R_a value of S0 is 1.86 μm, and a slight decrease can be observed in S1, about 1.50 μm after EBRTs in a momentary time. While for S2, R_a significantly drops to 0.12 μm due to the formation of the smooth surface by a sustained treated time. Consequently, the above micrographs observed by SEM reveal that EBRTs can change the microstructures of the W coatings controllably and
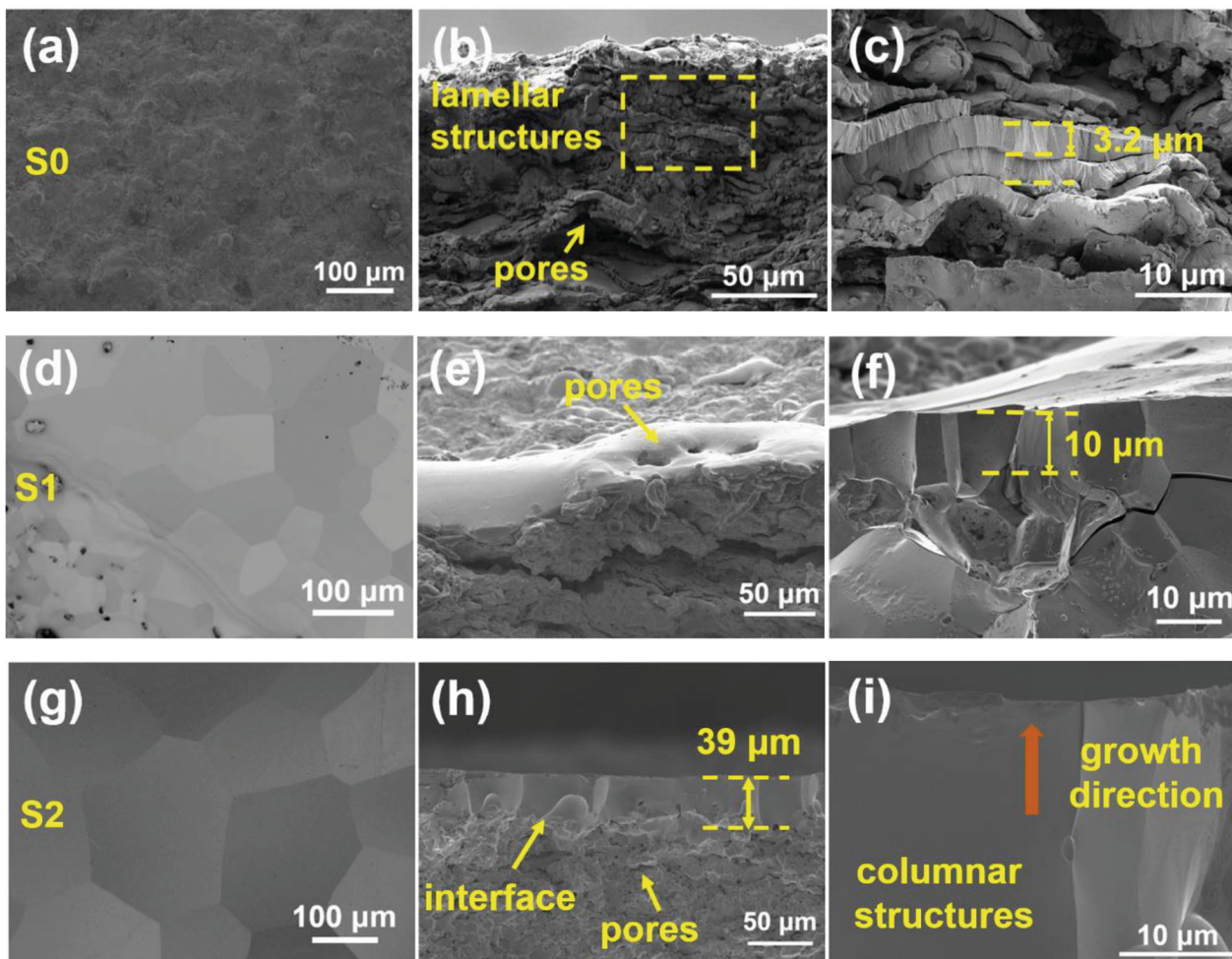
Fig. 2 SEM images of the detailed microstructures of S0, S1, and S2. (a) surface microstructure of S0, (b) cross-section microstructure of S0, (c) detailed lamellar structures of S0; (d) surface microstructure of S1; (e) cross-section microstructure of S1; (f) detailed columnar structures of S1; (g) surface microstructure of S2; (h) cross-section microstructure of S2; (i) detailed columnar structures of S2

Table 3 Surface roughness and electrochemical results of S0, S1, and S2 in the 3.5 wt.% NaCl solution with a scan rate of 1 mV/s

Sample	S0	S1	S2	W bulk
R_a, μm	1.859	1.500	0.12	…
I_c, μA/cm^2	7.86×10^{-1}	1.37×10^{-4}	8.66×10^{-18}	18.92
V_c, V	-0.2454	-0.3680	-0.1573	-0.2340

R_a: surface roughness; V_c: corrosion potential; I_c: corrosion current density

efficiently by adjusting the treating time and heat flux value and lead to a noticeable decrease in the surface roughness and porosity.

Porosity and Oxygen Content

Figure 3(a) further quantitatively displays the evolution of the porosity of S0, S1, and S2 after EBRTs, and Fig. 3(b) represents the microstructural images used to evaluate the porosity of the coatings. Initially, the as-sprayed W coating S0 has a relatively high porosity of about $3.9 \pm 0.3\%$ due to the intrinsic characteristics of the APS technique (Ref 31), which can be observed in the microstructure as shown in Fig. 2(b); then after EBRTs on S0 in a momentary time, the porosity decreases to about $1.6 \pm 0.5\%$ in S1, and further after a sustained treated time, the porosity decreases to extremely low in S2, about $0.2 \pm 0.1\%$, showing a significant reduction as compared with S0. Meanwhile, it was also found that the surface color of the W coating changes significantly. The as-sprayed W coating S0 presents a black surface and gradually becomes silvery white after being remelted. Finally, a
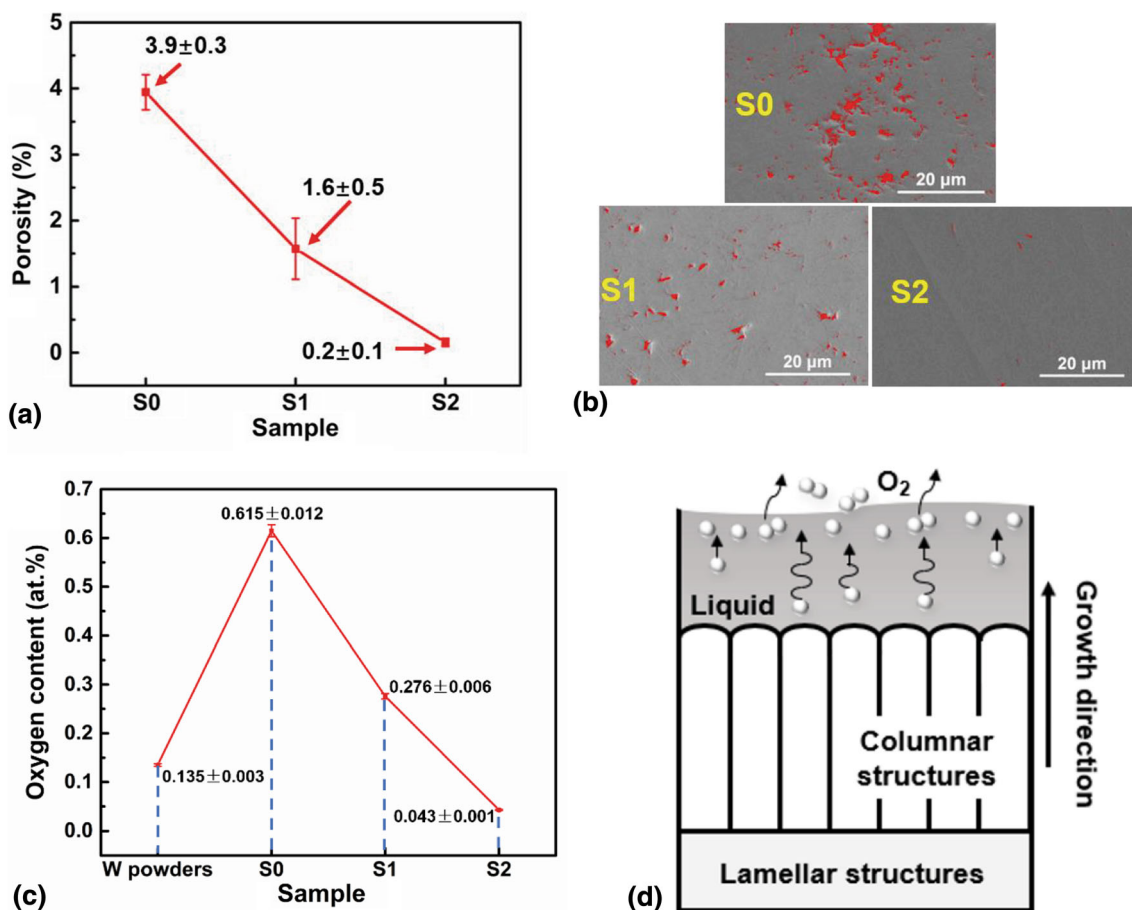
Fig. 3 (a) Comparison of the porosity of S0, S1, and S2; (b) microstructural images used to evaluate the porosity of the S0, S1, and S2; (c) oxygen content of W powders, S0, S1, and S2; (d) mechanism of oxygen evolution in the W coating during EBRTs

light metallic luster can be clearly observed on the surface after a sustained treated time. This can be mainly ascribed to the decrease of oxygen content in the W coatings, as shown in Fig. 3(c). There is about 0.615 ± 0.012 at.% oxygen in the as-sprayed W coating S0, and this value is even higher than that of the original W powers. This is because oxygen was introduced into the W coating during the sample preparation via the APS technique. After that, the oxygen content decreases dramatically by EBRTs. During the electron beam melting process, a temperature gradient was formed perpendicular to the surface of the W coating, and a non-equilibrium solidification occurred in the molten coating, and columnar crystals grew from bottom to top. Meanwhile, the solute oxygen atoms were excluded from the coating to the melted liquid, recombined into oxygen molecules, then transported onto the melted surface and evaporated, as shown in Fig. 3(d). After multiple remelting by electron beams, the oxygen content of the W coating dropped significantly. In the current study, a relatively small difference in oxygen content can be found between S1 and S2, 0.276 ± 0.006 at.% for S1 and 0.043 ± 0.001 at.% for S2, but after the analyses of these

two values independently, the oxygen content of S1 is almost as six times as that of S2. The oxygen content in S2 is even lower than the original powders. This is mainly due to the longer processing time of the S2 sample by EBRTs, and the oxygen can be fully released from the coatings. Therefore, both the porosity and oxygen content of the W coatings have reduced significantly after EBRTs, and these results also indicate that the porosity and oxygen content of the W coatings are controllable by EBRTs. Solving the inherent drawbacks of as-sprayed W coatings, such as high oxygen content and porosity, which directly affect the mechanical and physical properties of the coatings can give more possibility for the W coatings using as the plasma-facing materials in the first wall.

Phase Information

Figure 4(a) shows the XRD patterns of the original W powders, S0, S1, and S2. It can be seen that the W coatings maintain a single body-centered cubic (BCC) phase structure without any prominent oxide before and after the EBRTs. However, observing the first main peak by
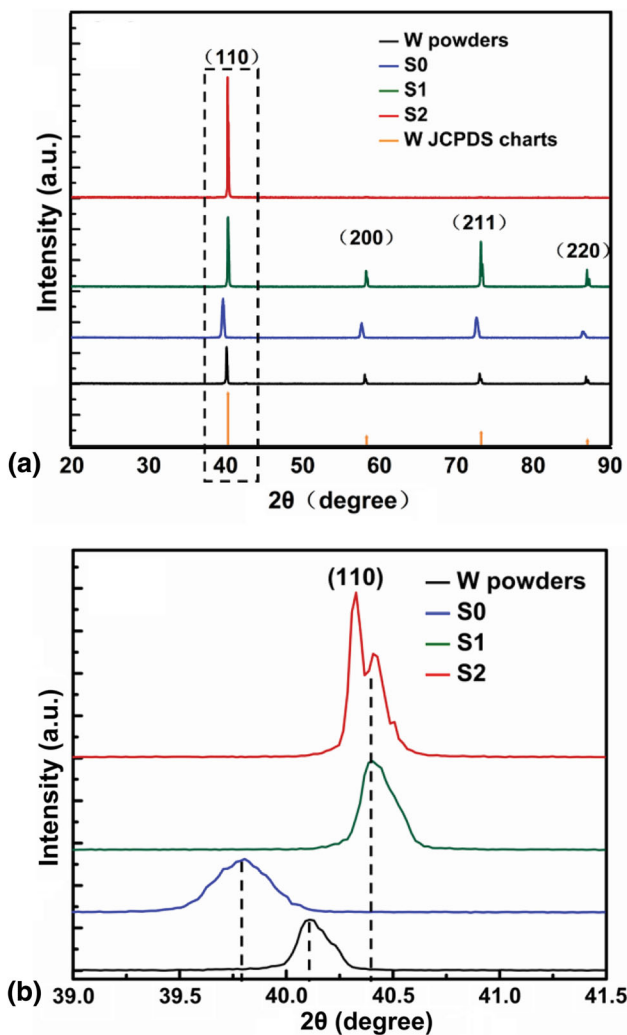
Fig. 4 (a) XRD patterns of W powders, S0, S1, and S2; (b) partial amplified the first peaks marked in (a)

Fig. 5 Comparison of the mechanical properties of S0, S1, and S2. (a) Cross-section microhardness; (b) the mass loss during wear resistance tests

zooming in, as shown in Fig. 4(b), it was observed the first peak position has shifted some certain angles in the different samples. This peculiar phenomenon is ascribed to the solid dissolved oxygen content in the W coating samples. In the beginning, the original W powders contained some oxygen, and then after preparing the W coatings by APS, more oxygen atoms were dissolved into the tungsten BCC crystal structure, resulting in the lattice distortion to a larger size and the XRD peak shifting towards the left. After EBRTs in a vacuum environment, the oxygen content in the W coatings declined dramatically, and the lattice structure shrank, leading to the peak shifting towards the right. These XRD test results matched quite well with the change of oxygen content, shown in Fig. 3(c). Meanwhile, an apparent preferential growth of the (110) crystal plane can be found in S2, and this is consistent with the growth of the columnar crystal structures observed by SEM, as exhibited in Fig. 2(h) and (i).
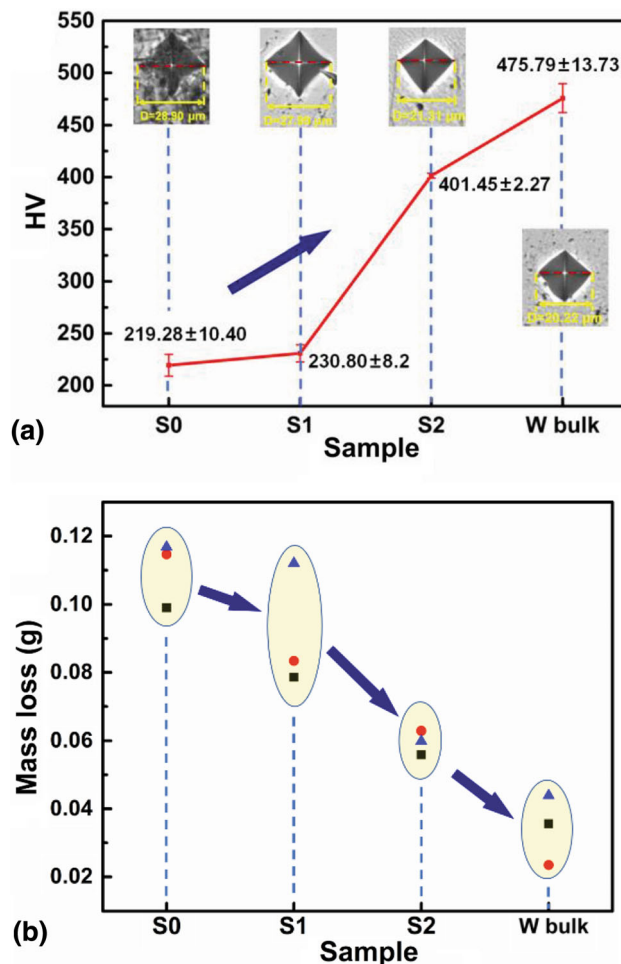
Mechanical and Physical Properties of the W Coatings Before and After EBRTs

Figure 5(a) displays the microhardness of the cross-section of the W coating before and after EBRTs. Each data point in Fig. 5(a) represents the average value of six indentation measurements, and the error bars represent the standard deviation values obtained. It can be seen that the microhardness of the W coatings increased significantly by EBRTs, from 219.28 ± 10.4 HV to 401.45 ± 2.27 HV, approaching the value of the bulk W sample. And the size of the indentation mark left on the surface of the coating is also getting smaller and smaller. The increase in microhardness is related to the densification of the coating microstructure and the decrease in porosity, which were precisely improved by the electron beam remelting process that can provide a rapid melting and solidification of the coating (Ref 32, 33). It is worth mentioning that a momentary treatment induced a gentle influence on the

microhardness, while significant change could be generated by a sustained treated time. For S2 samples, as exhibited in Fig. 2(h) and 3, a more homogeneous and compact surface remelting layer with low porosity and oxygen content can be found, which can have a positive impact on the mechanical performance. However, for S1 samples, the remelted layer is not uniform, and the microhardness is significantly affected by the below as-sprayed W coating due to the unclear interface between the remelted layer and the below as-sprayed W coating. This evolution has also coincided with the W coatings' wear resistance, as shown in Fig. 5(b). S0 exhibits 0.1068 g mass loss on average during a 20 s test; in contrast, the mass loss of S2 is around 0.0559 g, only half the value of S0. As the microstructures of the W coatings mostly transformed from lamellar to columnar structures by EBRTs in a sustained treated time, a remelting layer was formed on the whole coating surface with extremely low surface roughness and porosity, which can significantly reduce the mass loss during the test. A large fluctuation of mass loss values could be observed for S1 because of the uneven heating on the surface in momentary treated time, which can also influence the surface roughness level and mechanical erosion resistance. Previous studies showed that surface roughness of the coating could play an essential role in wear behaviors, and the mass loss rate of the coating becomes higher if it has a higher surface roughness (Ref 34-36). The tungsten lamella peeled off causes the W coating failure and mass loss, and the typical lamellar microstructure of the W coating is an important factor to induce its deterioration of abrasion wear resistance. As a result, although the oxygen content and the porosity had an obvious decline after EBRTs in a momentary time, only small changes of microstructures have been observed, resulting in a slight increment of microhardness and wear resistance. Overall, an improvement in the microhardness and wear resistance of the W coatings can be found after EBRTs, especially in a sustained treated time, which can eliminate lamellar microstructures, and it could effectively enhance the service life of the W coatings as a whole component during application.

In order to elucidate the effect of EBRTs on the corrosion properties of the W coatings, electrochemical corrosion investigations were performed on the W coatings. Figure 6(a) shows the comparison of corrosion behaviors of S0, S1, S2, and bulk W samples, and the electrochemical results are present in Table 3. It is encouraging to see that the corrosion current density I_c of the W coating has been reduced by orders of magnitude after EBRTs. In a momentary treated time, the current density I_c is reduced from 7.86×10^{-1} μA/cm^2 of S0 to 1.37×10^{-4} μA/cm^2 of S1, and after a sustained treated time, this current density I_c can further decrease to 8.66×10^{-18} μA/cm^2 of S2.
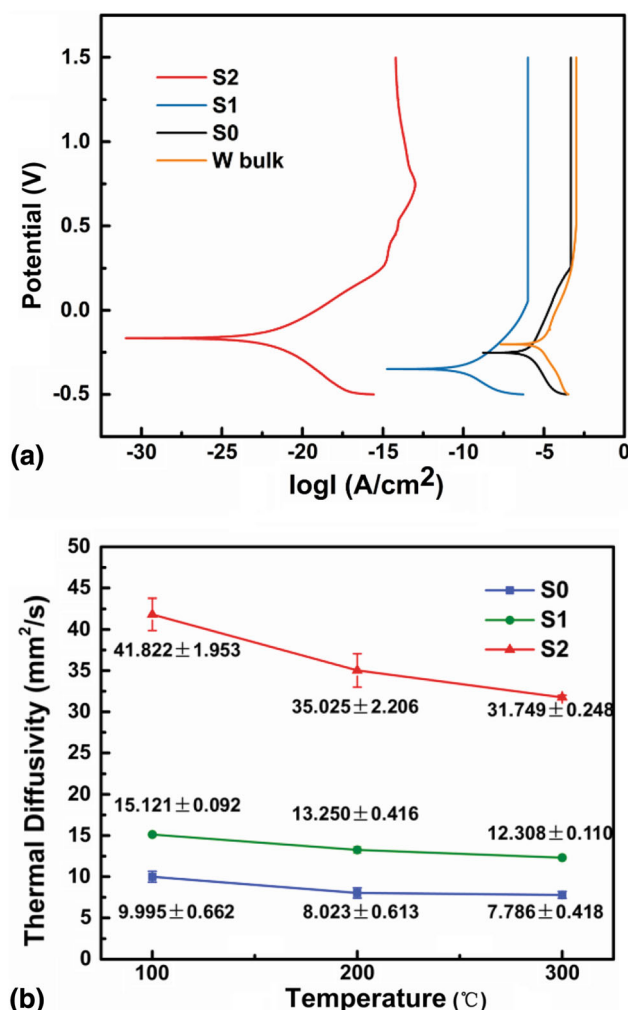

Fig. 6 (a) Potentiodynamic polarization curves during corrosion resistance tests; (b) thermal diffusivity at 100, 200, and 300 °C, respectively

The open-circuit potential (OCP) was from − 0.1 to 0.1 V, and the corrosion potential V_c was improved to − 0.1573 V for S2, as compared with − 0.2454 V for the S0 sample. While for the S1 sample, a decline could be found, which was − 0.3680 V. The corrosion behaviors show significant differences among S0, S1, and S2 due to their different microscopic corrosion mechanism, and the corrosion-resistant of the coating has been dramatically improved after EBRTs. In fact, the corrosion resistance of the coating was greatly affected by its microstructure, which has been reported previously (Ref 37). For S2, the corrosion mainly happened along the grain boundaries, and it was hard to find the corrosion traces in the grain; while for S1, the corrosion was not uniform and was prone to take place near the pores and grain boundaries; Severe corrosion behaviors can be found in the as-sprayed W coatings S0, which cause peeling on the surface to some extent. The surface morphologies of the S0, S1, and S2 coatings after
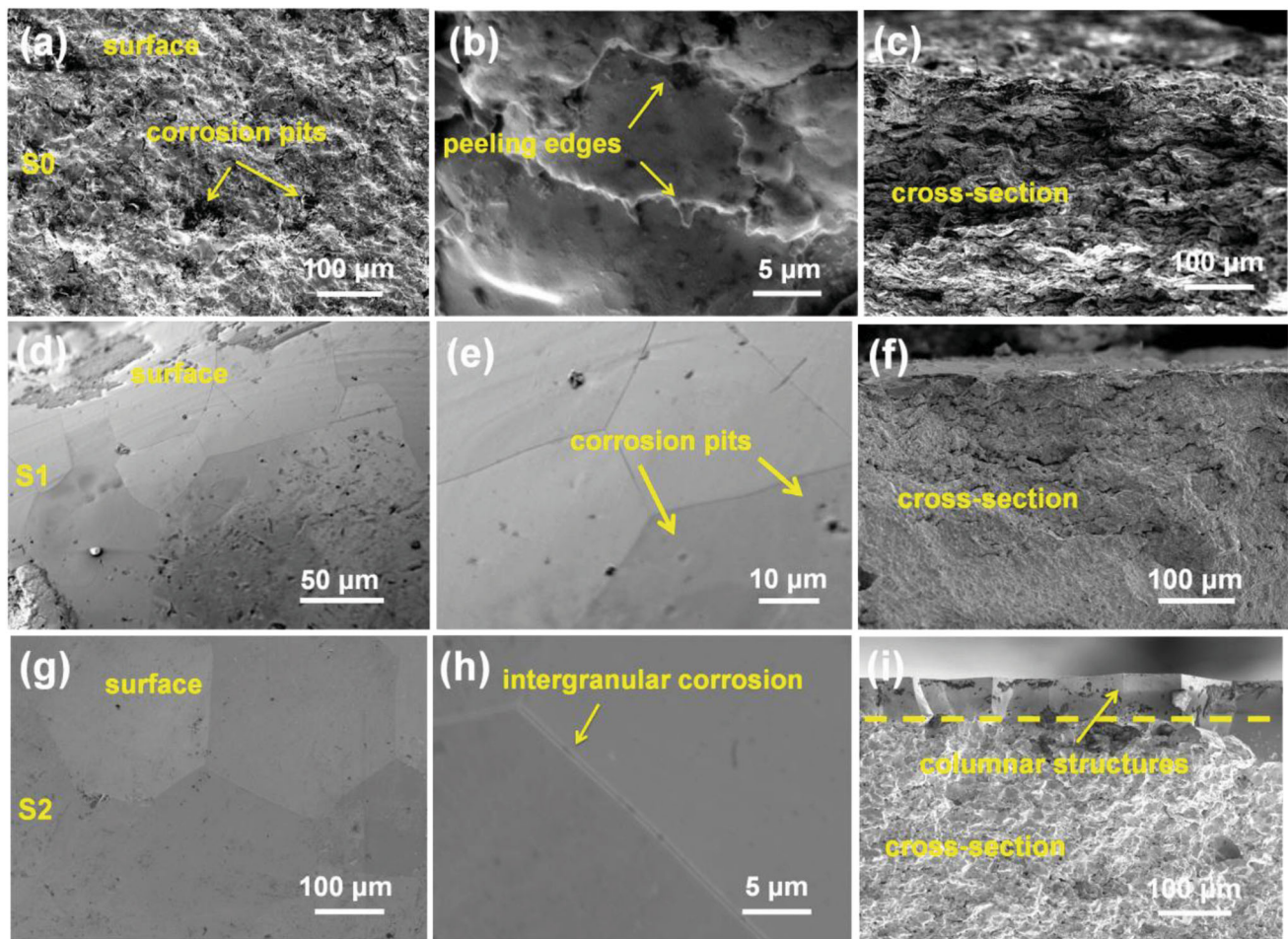
Fig. 7 SEM images of the detailed microstructures of S0, S1, and S2 after electrochemical corrosion. (a) Surface corrosion microstructure of S0, (b) detailed peeling edges of S0, (c) cross-section corrosion microstructure of S0; (d) surface corrosion microstructure of S1, (e) detailed corrosion structure of S1, (f) cross-section corrosion microstructure of S1; (g) surface corrosion microstructure of S2, (h) detailed intergranular corrosion structure of S2, (i) cross-section corrosion microstructure of S2

being subjected to the polarization test in 3.5 wt.% NaCl solution was examined using SEM, as shown in Fig. 7. The surface of the S0 coating was completely covered with defects and micro-pits (Fig. 7a), with some large pitting holes being corroded to the extent that peeling edges were formed (Fig. 7b); however, the majority of the S1 surface was covered by micro-pits, as shown in Fig. 7(d) and (e). Meanwhile, several corrosion-induced small pitting holes were observed on the surface of S2, and localized intergranular corrosion occurred, as shown in Fig. 7(g) and (h), which verified its superior corrosion resistance as compared to the S0 and S1 coatings. From the cross-section micrographs of S0, S1, and S2 after corrosion tests, as shown in Fig. 7(c), (f), and (i) respectively, it is hard to observe the difference before and after the corrosion of each sample, which is mainly because the corrosion occurs on the surface. Nevertheless, it is worth noting that the columnar crystalline structures formed on the surface of the

S2 coating after EBRTs play a very active role in corrosion protection.

Due to the W coatings would be exposed as the plasma-facing materials for use in the first wall of nuclear fusion devices, the thermal diffusivity was a critical parameter that should be taken into consideration. Thus we further investigated the influence of the EBRTs on the thermal diffusivity of the W coatings by the flash method. The thermal diffusivity of S0, S1, and S2 are investigated at three different temperatures of 100, 200, 300 °C, respectively, as shown in Fig. 6(b). At 100 °C, S0 has a thermal diffusivity of 9.995 ± 0.662 mm^2/s, and after a momentary treated time by EBRTs, the thermal diffusivity increases to 15.121 ± 0.092 mm^2/s for S1. In contrast, after a sustained treated time, the thermal diffusivity of S2 reaches 41.822 ± 1.953 mm^2/s, implying that the W coating after EBRTs has higher efficiency to reach a uniform temperature during heating or cooling. The EBRTs were an effective way/method to improve the thermal diffusivity of

the W coatings. It was confirmed that the porosity of the coatings had a significant influence on the thermal diffusivity, and a low porosity often led to a high thermal diffusivity (Ref 38). In the current study, the porosity of the W coating has been reduced dramatically by EBRTs, resulting that S1 or S2 has a higher thermal diffusivity value as compared with S0 at each temperature, and with a sustained treating time, the remelted layer becomes much denser, thus a much higher thermal diffusivity value can be seen in S2. For the S1 sample with a momentary treating time, an inhomogeneous remelted layer was formed on the surface. It had a higher porosity than S2, which would negatively influence the thermal diffusivity resulting in a lower thermal diffusivity of S1 than S2. Moreover, it can be seen that the thermal diffusivity of S0 and S1 remains relatively stable and decrease slightly with increasing the sample temperature. In contrast, for S2, the thermal diffusivity decreases more as the temperature increases. This case can be attributed to the different oxygen content of the samples. It was reported that the fewer impurity elements contained in W metal, the more the thermal diffusivity decreases with the temperature increases, as impurity elements would affect the electron in W metal (Ref 39-41). Since after EBRTs in a sustained treated time, the oxygen content in S2 has been reduced to an extremely low level, and the thermal diffusivity of S2 would decrease rapidly with increasing temperature.

The above experimental results demonstrate that the W coatings after EBRTs show outstanding mechanical properties, corrosion resistance, and thermal diffusivity. EBRTs could be an efficient path to modify and control their microstructures and improve their mechanical properties. Comparing with the traditional as-sprayed W coatings, they are more suitable for practical application in future nuclear fusion devices. Although much work remains to optimize the W coating for application, for example, the bonding strength under heat load, the extraordinary properties of the W coating after EBRTs reported here offer a strong motivation to pursue their development.

Conclusions

In summary, we investigated the microstructural evolution and the performances of W coatings upon EBRTs with a momentary time and a sustained time. The as-sprayed W coating showed many pores and typical small lamellar microstructures with a simple BCC phase structure. After EBRTs, a compact remelted layer with columnar crystal structure was formed on the surface of the W coatings. Subsequently, EBRTs in a sustained time, the porosity of the W coatings was significantly reduced from 3.9 ± 0.3 to $0.2 \pm 0.1\%$, and the oxygen content decreased from

0.615 ± 0.012 at.% to 0.043 ± 0.001 at.%. It was found that the microhardness of the W coatings increased from 219.28 ± 10.40 HV to 401.45 ± 2.27 HV after EBRTs. Meanwhile, wear resistance, corrosion resistance, and thermal diffusivity of the W coatings had also been significantly improved after EBRTs. The improvement of these properties is mainly due to the change of microstructure and the reduction of porosity and oxygen content in the W coatings by EBRTs. Furthermore, the surface modification process for the W coating is fast and controllable: the thickness of the coating, treating time, heat flux can be tuned. These experimental results demonstrated that EBRTs could be used as an effective and controllable surface modification technique for coatings. Although the modification is limited by the penetration depth of the electron beams, a controllable treatment with a sustained time and a high energy density can be used to address these issues. To our knowledge, this work constitutes the first report of the W coating by EBRTs, and it could open new opportunities for using EBRTs to functionalize other coating materials with better performance.

Data availability statement The raw/processed data that support the findings of this study are available on request from the corresponding author.

Declaration

References

1. L. Sandoval, D. Perez, B.P. Uberuaga and A.F. Voter, Formation of Helium-Bubble Networks in Tungsten, *Acta Mater.*, 2018, **159**, p 46-50.
2. V. Philipps, Tungsten as Material for Plasma-Facing Components in Fusion Devices, *J. Nucl. Mater.*, 2011, **415**, p S2-S9.
3. N. Yoshida, Review of Recent Works in Development and Evaluation of High-Z Plasma Facing Materials, *J. Nucl. Mater.*, 1999, **266-269**, p 197-206.
4. Y. Ueda, J.W. Coenen, G.D. Temmerman, R.P. Doerner, J. Linke, V. Philipps and E. Tsitrone, Research Status and Issues of Tungsten Plasma Facing Materials for ITER and Beyond, *Fusion Eng. Des.*, 2014, **89**, p 901-906.

5. X.L. Jiang, F. Gitzhofer and M.I. Boulos, Thermal Spray Coating of Tungsten for Tokamak Device, *Plasma Sci. Technol.*, 2006, **8**, p 164-167.

6. J. Matějíček, P. Chráska and J. Linke, Thermal Spray Coatings for Fusion Applications-Review, *J. Therm. Spray Technol.*, 2007, **16**, p 64-83.

7. F. Ferroni, X. Yi, K. Arakawa, S.P. Fitzgerald, P.D. Edmondson and S.G. Roberts, High Temperature Annealing of Ion Irradiated Tungsten, *Acta Mater.*, 2015, **90**, p 380-393.

8. K. Wang, M.E. Bannister, F.W. Meyer and C.M. Parish, Effect of Starting Microstructure on Helium Plasma-Materials Interaction in Tungsten, *Acta Mater.*, 2017, **124**, p 556-567.

9. L. Begrambekov, A. Gordeev, Y. Ma, G. Vayakis, P. Shigin, Y. Sadovsky, A. Zakharov and M. Walsh, Development of Quality Tungsten Coating on Ceramics as a Microwave Shield for ITER High-Frequency Magnetic Sensor, *Fusion Sci. Technol.*, 2020, **76**, p 1-12.

10. N.B. Sun, S.T. Lang, Y.C. Zhang, Y.P. Xu, H. Liu and G.B. Li, Properties of Electrodeposited Tungsten Coatings on Graphite Substrates for Plasma Facing Components, *J. Fusion Eng.*, 2016, **35**, p 660-665.

11. H.S. Kim, B.R. Kang, H.M. Lim, S.Y. Moon and B.G. Hong, Tungsten Coatings and Heat/Particle Flux Test by the Vacuum Plasma Spray System, *J. Nanosci. Nanotechnol.*, 2017, **17**, p 8457-8461.

12. A. Cambe, E. Gauthier, J.M. Layet and S. Betivegna, Development of Tungsten Coating for Fusion Applications, *Fusion Eng. Des.*, 2001, **56-57**, p 331-336.

13. O. Kovářík, P. Haušild and J. Siegl, The Influence of Substrate Temperature on Properties of APS and VPS W Coatings, *Surf. Coat. Technol.*, 2015, **268**, p 7-14.

14. Q.Y. Hou, L.M. Luo, Z.Y. Huang, P. Wang, T.T. Ding and Y.C. Wu, Comparison of W-TiC Composite Coatings Fabricated by Atmospheric Plasma Spraying and Supersonic Atmospheric Plasma Spraying, *Fusion Eng. Des.*, 2016, **105**, p 77-85.

15. D.Y. Hu, X.B. Zheng, Y.R. Niu, H. Ji, F.L. Chong and J.L. Chen, Effect of Oxidation Behavior on the Mechanical and Thermal Properties of Plasma Sprayed Tungsten Coatings, *J. Therm. Spray. Technol.*, 2008, **17**, p 377-384.

16. Z.J. Zhou, S.X. Song, W.Z. Yao, G. Pintsuk, J. Linke, S.Q. Guo and C.C. Ge, Fabrication of Thick W Coatings by Atmospheric Plasma Spraying and Their Transient High Heat Loading Performance, *Fusion Eng. Des.*, 2010, **85**, p 1720-1723.

17. F. Wang and J.J. Huang, Performance Characterization and Improvement of Tungsten Coating Atmospheric Plasma Sprayed with Submicron Powder, *Surf. Coat. Technol.*, 2014, **254**, p 61-64.

18. J.J. Huang, F. Wang, Y. Liu, S.S. Jiang, X.S. Wang, B. Qi and L. Gao, Properties of Tungsten Coating Deposited onto Copper by High-Speed Atmospheric Plasma Spraying, *J. Nucl. Mater.*, 2011, **414**, p 8-11.

19. F.L. Chong, J.L. Chen, J.G. Li, D.Y. Hu and X.B. Zheng, Heat Load Behaviors of Plasma Sprayed Tungsten Coatings on Copper Alloys with Different Compliant Layers, *J. Nucl. Mater.*, 2008, **375**, p 213-217.

20. J. Matějíček and P. Holub, Laser Remelting of Plasma-Sprayed Tungsten Coatings, *J. Therm. Spray Techn.*, 2014, **23**, p 750-754.

21. D. Utua, W. Brandl, G. Marginean, I. Cartis and V.A. Serban, Morphology and Phase Modification of HVOF-Sprayed MCrAlY-Coatings Remelted by Electron Beam Irradiation, *Vaccum*, 2005, **77**, p 451-455.

22. P. Petrov, Electron Beam Surface Remelting and Alloying of Aluminium Alloys, *Vaccum*, 1997, **48**, p 49-50.

23. H.P. Tang, M. Qian, N. Liu, X.Z. Zhang, G.Y. Yang and J. Wang, Effect of Powder Reuse Times on Additive Manufacturing of Ti-6Al-4V by Selective Electron Beam Melting, *JOM*, 2015, **67**, p 555-563.

24. S. Zhao, S.J. Li, S.G. Wang, W.T. Hou, Y. Li, L.C. Zhang, Y.L. Hao and R. Yang, Compressive and Fatigue Behavior of Functionally Graded Ti-6Al-4V Meshes Fabricated by Electron Beam Melting, *Acta Mater.*, 2018, **15**, p 1-15.

25. Y.Z. Wu, W.B. Liao, F. Wang, M.L. Wang, C.Y. Yu, Z. Wang, Z.X. Guo, Z.Y. Liu, Y.B. Cao and J.J. Huang, Effect of Electron Beam Remelting Treatments on the Performances of Plasma Sprayed Zirconia Coatings, *J. Alloy Compd.*, 2018, **756**, p 33-39.

26. G.Y. Yang, P.W. Yang, K. Yang, N. Liu, L. Jia, J. Wang and H.P. Tang, Effect of Processing Parameters on the Density, Microstructure and Strength of Pure Tungsten Fabricated by Selective Electron Beam Melting, *Int. J. Refract. Met. H.*, 2019, **84**, p 105040.

27. M. Galati and L. Iuliano, A Literature Review of Powder-Based Electron Beam Melting Focusing on Numerical Simulations, *Addit. Manuf.*, 2018, **19**, p 1-20.

28. D. Tomus and M. Qian, Electron Beam Processing of Al-2Sc Alloy for Enhanced Precipitation Hardening, *Scr. Mater.*, 2010, **63**, p 151-154.

29. M.D. Abràmoff, P.J. Magalhães and S.J. Ram, Image Processing with ImageJ, *Biophot. Int.*, 2004, **11**, p 36-42.

30. F. Wang, G.N. Luo, J.J. Huang and Y. Liu, Properties Improvement of Atmospheric Plasma Sprayed Tungsten Coating by Annealing, *Surf. Coat. Technol.*, 2019, **358**, p 276-281.

31. Z.J. Zhou, S.Q. Guo, S.X. Song, W.Z. Yao and C.C. Ge, The Development and Prospect of Fabrication of W Based Plasma Facing Component by Atmospheric Plasma Spraying, *Fusion Eng. Des.*, 2011, **86**, p 1625-1629.

32. A. Förg, A. Myrell, A. Killinger and R. Gadow, Suspension and Coating Characterization of High Velocity Suspension Flame Sprayed (HVSFS) Mixed Titanium Oxide-Titanium Carbide Coatings, *Surf. Coat. Technol.*, 2019, **371**, p 90-96.

33. Y.X. Chen, J.C. Shang, X.B. Liang, H.X. Wang and Z.D. Zhou, Warm-Particle Peening Assisted HVOF Spraying: A New Process to Improve the Coating Performances, *Surf. Coat. Technol.*, 2019, **367**, p 135-147.

34. M.F. Buchely, J.C. Gutierrez, L.M. León and A. Toro, The Effect of Microstructure on Abrasive Wear of Hardfacing Alloys, *Wear*, 2005, **259**, p 52-61.

35. R. Gheisari and A.A. Polycarpou, Three-Body Abrasive Wear of Hard Coatings: Effects of Hardness and Roughness, *Thin Solid Films*, 2018, **666**, p 65-67.

36. J. Sudagar, J.S. Lian, Q. Jiang, Z.H. Jiang, G.Y. Li and R. Elanszezhian, The Performance of Surfactant on the Surface Characteristics of Electroless Nickel Coating on Magnesium Alloy, *Prog. Org. Coat.*, 2012, **74**, p 788-793.

37. M. Popczyk, J. Kubisztal, A.S. Swinarew, Z. Waśkiewicz, A. Stanula and B. Knechtle, Corrosion Resistance of Heat-Treated Ni-W Alloy Coatings, *Materials*, 2020, **13**, p 1172.

38. F. Cernuschi, P. Bianchi, M. Leoni and P. Scardi, Thermal Diffusivity/Microstructure Relationship in Y-PSZ Thermal Barrier Coatings, *J. Therm. Spray Technol.*, 1999, **58**, p 102-109.

39. T. Tanabe, C. Eamchotchawalit, C. Busabok, S. Taweethavorn, M. Fujitsuka and T. Shikama, Temperature Dependence of Thermal Conductivity in W and W-Re Alloys from 300 to 1000 K, *Mater. Lett.*, 2003, **57**, p 2950-2953.

40. J. Habainy, Y. Dai, Y.J. Lee and S. Iyenga, Thermal Diffusivity of Tungsten Irradiated with Protons up to 5.8 dpa, *J. Nucl. Mater.*, 2018, **509**, p 152-157.

41. A. Reza, Y. Zayachuk, H.B. Yu and F. Hofmann, Transient Grating Spectroscopy of Thermal Diffusivity Degradation in Deuterium Implanted Tungsten, *Scr. Mater.*, 2020, **174**, p 6-10.